Diamond & Related Materials 143 (2024) 110926

Contents lists available at ScienceDirect

Diamond & Related Materials

journal homepage: www.elsevier.com/locate/diamond

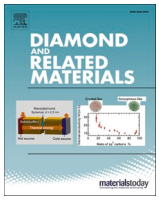

# Micron-scale Al particulates to improve the piezoresistive performance of amorphous carbon films

Shanze Liu [a,b], Zhihan Zhao [b], Wenlong Zhang [b], Rende Chen [b], Jing Wei [b], Peng Guo [b,*], Aiying Wang [b,c,**]

[a] College of Mechanical Engineering, Zhejiang University of Technology, Hangzhou 310000, China
[b] Key Laboratory of Marine Materials and Related Technologies, Zhejiang Key Laboratory of Marine Materials and Protective Technologies, Ningbo Institute of Materials Technology and Engineering, Chinese Academy of Sciences, Ningbo 315201, China
[c] Center of Materials Science and Optoelectronics Engineering, University of Chinese Academy of Sciences, Beijing 100049, China

ARTICLE INFO

*Keywords:*
Micron-scale Al particulates
Amorphous carbon films
Piezoresistive mechanism
Electric behavior

ABSTRACT

Amorphous carbon (a-C) has been extensively studied as a promising candidate for microelectromechanical system (MEMS) piezoresistive sensors owing to its excellent mechanical properties and sensitivity. However, the semiconductor features of a-C films complicate achieving a high gauge factor (GF) and low temperature coefficient of resistance (TCR). In this study, we introduced micron-scale Al particulates (2.4–5.2 μm average size) by dewetting before a-C deposition, which simultaneously improved the GF and reduced the TCR of the composite structure. An atomic bond analysis revealed that applying the Al particulates favored the formation of $sp^2$, thus reducing the localized surface potential of the a-C film. When the density of the Al particulates reached 15,000/$mm^2$, the GF (36.9) of the a-C film significantly increased by more than 350 %, whereas the TCR decreased as the average size of the Al particulates increased. Furthermore, the composite exhibited typical Schottky contact characteristics and formed a Schottky barrier of 0.43 eV at the Al/a-C contact interface. Carrier transport between the Schottky barriers was achieved by the holes (primary carriers) via tunnelling. These significant piezoresistive properties can be explained by the variation in the Schottky barrier height.

## 1. Introduction

Piezoresistive sensors have been gaining interest for application in several fields of microelectromechanical systems (MEMS), such as aerospace, biomedical, automobile, and oceanographic, especially owing to their combined advantages of an excellent sensitivity and repeatability as well as facile scaling-down for low-powered electronic devices [1]. However, with the rapid development of harsh environments including heavy wear, severely corrosive chloride media, and high radiative temperatures, traditional Si-based MEMS sensors suffer from the challenges of poor mechanical properties, low chemical inertness, and a narrow bandgap (~ 1.1 eV) [1]. Various wide bandgap semiconductors, including diamond, SiC, AlN, ZnO, and amorphous carbon (a-C), have been investigated as new piezoelectric materials for high-performance MEMS sensors owing to their excellent piezoelectric effect combined with outstanding electrical, mechanical, and chemical properties [2]. In particular, a-C films are one of the most well-known piezoelectric candidates, which are composed of diamond structures (C-$sp^3$) and hybridized graphitic carbon bonds (C-$sp^2$) [3,4]. By tailoring the atomic carbon bonds during film deposition, a-C films also possess a wide bandgap of up to 4 eV [5], excellent inertness in both acidic and alkaline solutions, a high hardness and Young's modulus [6,7], and promote a largely uniform facile synthesis. These unique characteristics enable a-C films to demonstrate remarkable piezoresistive effects [8–13], accompanied by a large gauge factor (GF) of up to 1200, highly integrated compatibility to the MEMS manufacturing process [12,13], utilization in the latest generation of flexible strain sensors [14], and a stronger availability under severe abrasion or a wide temperature range (−20–100 °C) [15,16].

Regardless, a key barrier to a-C piezoresistive films is their similar temperature sensitivity to that of typical Si materials, where the temperature coefficient of resistance (TCR) can be as high as −8000 ppm/K

* Corresponding author at: Key Laboratory of Marine Materials and Related Technologies, Zhejiang Key Laboratory of Marine Materials and Protective Technologies, Ningbo Institute of Materials Technology and Engineering, Chinese Academy of Sciences, Ningbo 315201, China.
** Correspondence to: A. Wang, Center of Materials Science and Optoelectronics Engineering, University of Chinese Academy of Sciences, Beijing 100049, China
*E-mail addresses:* guopeng@nimte.ac.cn (P. Guo), aywang@nimte.ac.cn (A. Wang).

https://doi.org/10.1016/j.diamond.2024.110926
Received 29 December 2023; Received in revised form 2 February 2024; Accepted 18 February 2024
Available online 19 February 2024

[9]. For counteracting the sensitive performance, doping metals with a positive TCR value into a negative amorphous carbon matrix has been applied to enhance the temperature-insensitive properties over a wide temperature range. For example, by incorporating Cu atom into a-C films, Meškinis et al. [17] found that the TCR value significantly reduced to −500 ppm/K, whereas the GF value simultaneously decreased to approximately 3.2. Comparatively, both GF and TCR underwent a non-monotonical increase or decrease in the Nb-doped a-C films, where a high GF of 35.5 combined with a TCR of −707 ppm/K, and a low GF of 10.9 combined with a TCR of −93 ppm/K, was obtained with Nb concentrations ranging between 20 and 72 at. % [18]. In this regard, a decrease in the TCR value without the simultaneous deterioration of the GF is critical to ensure that a-C films can be used as high-accuracy and piezoresistive materials for advanced MEMS sensors or actuators.

Based on the theoretical analysis, GF and TCR reflect the resistance changes with respect to the various environmental testing factors, namely the applied pressure, strain, and operating temperature. For a-C films and relative metal-doped amorphous carbon nanocomposite films, the piezoresistive mechanism was empirically proposed using the thick film resistance (TFR) model [19,20], where the material structure was treated as a nanocomposite with conductive $sp^2$ clusters or with doped metallic clusters embedded in an insulated C-$sp^3$ interlinked matrix. When extra stress/strain was applied, the distance between the conductive phases changed, resulting in a substantial difference in the electrical resistance and piezoresistive effect. However, as the operating temperatures changed, the characteristics of the carrier transport obeyed the hollow thermal activation or hopping models evolving with the electron/proton/hole. In particular, the concentrations and distributions of the doped metals or the formed nanoparticles demonstrated a strong influence on TCR-related behavior as well as the GF effect in a-C materials [21].

Previously, although both high GF at 20 and low TCR about 0 ± 50 ppm/K were obtained in hydrogenated a-C films by controlling the doped Ni concentration of 55 at.%, the difficulty was to establish the conductive pathway in a controllable way [20]. This challenge was mainly owing to the complexity of the approaches used in hybrid magnetron sputtering techniques, in which it was difficult to regulate the nanoparticle size and phase distribution by tailoring the doped metal atoms in the amorphous carbon matrix. To overcome the aforementioned problems, by using the mature dewetting features of metals [22–24], we fabricated a novel composite structure combining a bottom layer with micron-scale Al particulates and a functional a-C film by a hybrid ion beam method in this study. The concentration and size of the Al particulates were controlled by varying the thickness of the deposited Al films and the thermal annealing time. Dense a-C films were specially fabricated using a high-power impulse magnetron sputtering (HiPIMS) technique, which has a higher ionization rate and larger incident ion energy than those of traditional magnetron sputtering. The electrical properties of the a-C films coated on the Al micro-particulates were investigated at temperatures ranging between 200 and 400 K. The piezoresistive mechanism was also discussed in terms of the microstructural evolution and carrier transport characteristics of the fabricated a-C films.

## 2. Materials and methods

### 2.1. Preparation of micron-scale Al particulates

Fig. 1a presents a schematic diagram of the Al deposition. First, Al films with different thickness were deposited by a home-made direct current magnetron sputtering (DCMS) technique, in which a rectangular aluminum target with a purity of 99.99 wt% supplied the Al beam source. N-type silicon wafers with a ⟨100⟩ crystalline orientation with 300 nm thermal oxide layers on both sides were used as the substrates. Before the deposition of the Al films, the substrates were ultrasonically cleaned with acetone and anhydrous ethanol for 10 min, followed by drying under nitrogen. Subsequently, the substrates were fixed on the rotated substrate holder located in the deposition chamber. The distance between the substrate and Al target was approximately 8 cm. When the base pressure of the chamber was evacuated to $2 \times 10^{-5}$ Torr, $Ar^+$ ions generated from the linear ion source were used with a DC pulsed bias voltage of −200 V for the etching process, corresponding to the removal of contaminants adsorbed on the substrate surface for 20 min. Subsequently, Ar precursor gas was introduced to ignite the aluminum target for deposition of the Al film, along with a DC sputtering power at 0.1 kW and a working pressure at $1.5 \times 10^{-3}$ Torr. The thickness of the Al film, ranging between 40 and 100 nm, was adjusted by setting the deposition time to 14, 20, 26, and 32 min.

After deposition of the Al film, all the samples were placed in a tubular annealing furnace to generate micron-scale Al particulates (Fig. 1b). The vacuum during annealing was pumped to less than $1.5 \times 10^{-5}$ Torr. To ensure the complete dewetting of the Al film for the required particulates, the samples that underwent deposition for 14 min were annealed at 600 °C for 3 h, whereas those that underwent deposition for 20, 26, and 32 min were annealed at 650 °C for 3 h, followed by slowly cooling them to room temperature in the furnace.

### 2.2. Deposition of a-C film

As shown in Fig. 1c, the a-C film was deposited using the homemade HiPIMS technique composed of a rectangular graphite target with dimensions of 380 mm × 100 mm × 7 mm (purity 99.99 %). The treated

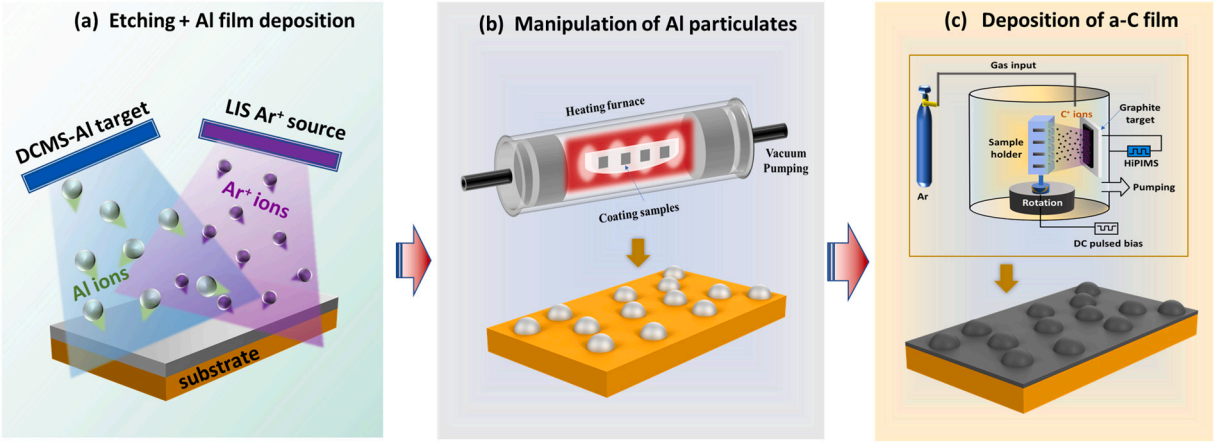


**Fig. 1.** Schematic of the fabrication process of the unique Al/a-C composites. (a) Al film deposition, (b) Al micron- particulate manipulation, and (c) a-C film deposition.

silicon oxide wafers with and without the produced micron-scale Al particulates were used as substrates for comparison. In this process, the distance between the substrate and sputtered graphite target was approximately 15 cm to enhance the uniformity of the film. When the basic pressure reached $2 \times 10^{-5}$ Torr, the substrates were precleaned by the $Ar^{+}$ ions from the linear ion source for 5 min, with the other operating parameters being the same as those of the Al deposition. Ionization of the graphite target was then conducted under an Ar gas flow rate of 100 sccm for the growth of the a-C film using the unique mode of the HiPIMS technique. The magnetron sputtering power was 500 W, and the pulse duty ratio and pulse width was set at 0.1 and 200 μs, respectively. During a-C deposition, a DC pulsed bias of −200 V was applied to the substrate to enhance the adhesion strength. The working pressure was maintained at $8 \times 10^{-3}$ Torr and the deposition time was 160 min, with its corresponding thickness around 200 ± 10 nm. For simplicity, S1 indicates the pure a-C films, whereas S2–S5 indicate the a-C films with various micron-scale Al particulates under deposition times of 14, 20, 26, and 32 min, respectively.

### 2.3. Characterization method

The thicknesses of the Al and a-C films were determined by measuring the marked step height using a surface profilometer (Alpha-Step IQ, US). The surface morphology of the Al film after annealing was examined by scanning electron microscopy (SEM, FEI Quanta FEG 250, USA). Confocal micro-Raman spectroscopy (Renishaw inVia Reflex, UK, 532 nm) was used to identify the atomic carbon bonds in the a-C films for a non-destructive analysis. The cross-sectional morphologies and microstructures of the deposited films were studied using transmission electron microscopy (TEM; Tecnai F20, USA). Electron energy loss spectroscopy (EELS) was used to investigate the $sp^2/sp^3$ fraction in the deposited a-C film using highly oriented pyrolytic graphite (HOPG, 100 % $sp^2$-C bonds) as a reference. Samples for the TEM and EELS tests were prepared using focused ion beam technology (FIB, Carl Zeiss Auriga, Germany).

The I-V plots of the films at temperatures ranging between 200 and 400 K were characterized by a physical property measurement system (PPMS, Quantum Design, Model-9), whereas the work function was investigated by ultraviolet photoelectron spectroscopy (UPS, Axis Ultra DLD, Jap). The UPS spectrum was measured using a He I (21.22 eV) light source and the spectrometer was calibrated with respect to the Fermi edge of the clean Ag sample. The optical band gap of the a-C film was studied using diffuse reflectance spectroscopy measured by a UV–visible near-infrared spectrometer (UV/Vis/NIR Spectrometer, Lambda 950, USA) at wavelengths ranging between 175 and 2500 nm. The effect of introducing Al particles on the conductive path of the sample surface was observed by the Kelvin probe force microscopy (KPFM) mode of a scanning probe microscope (Dimension ICON, Bruker, USA), which revealed the distribution of the surface charges on the samples.

A homemade device was employed to measure the GF of the a-C films using a three-point method. Fig. 2a presents a schematic of the testing device, which consisted of a support sample table, loading mechanism (Atterberg, HP-50 N), dial gauge, and recorded digital multimeter (FLUKE, 8846 A). As shown in Fig. 2b, during the measurement, the test sample was first fixed on the sample table, which was followed by applying a strain/stress onto the center of the sample with a loading mechanism. Simultaneously, the change in the vertical position of the indenter (ΔY), initial resistance ($R_0$), and change in the resistance (ΔR) was detected by the dial gauge and digital multimeter, respectively. Subsequently, the GF of the a-C film was calculated using Eq. (1) [25]:

$$GF = \frac{\Delta R}{R_0 \varepsilon} = \frac{l^2}{3t\Delta Y} \bullet \frac{\Delta R}{R_0} \quad (1)$$

Here, the total thickness of the test sample was recorded as *t*; and the distance between the two support points on the sample stage was assigned as the effective length l. The effective length was set to approximately 30 mm in the test.

## 3. Results and discussion

### 3.1. Surface morphologies and microstructures

Fig. 3 presents the surface morphologies of the Al films with various thicknesses after thermal annealing. Excluding the samples with varied morphologies, all those treated exhibited typical spherical micron-scale Al particulates owing to the intrinsic property resulting from metal dewetting (Fig. 3a-d). As the Al film thickness increased from 40 to 100 nm, the diameter of the formed Al particulates gradually increased. Specifically, the average size of the Al particulates increased from 2.37 μm for sample S2 to 5.2 μm for S5, as demonstrated by the images in Fig. 3 a-d. However, the density of the Al particulates exhibited an initial increase followed by a subsequent decrease, indicating that the highest particulate density of 15,000/$mm^2$ was observed in sample S3. Fig. 3e presents the representative EDS analysis of S3, demonstrating that only the apperance of the Al element was distributed in the formed particulates. In addition, analyzing the cross-sectional surface of the sample after annealing by high resolution transmission electron microscopy (HRTEM) demonstrated the distinct interfaces, including the $Si/SiO_2$ substrate and amorphous a-C feature, which can be attributed to the corresponding SAED pattern with a diffuse halo (Fig. 3f-g). This observation is typical of amorphous carbon films and implies full dewetting of the bottom Al films.

The impact of the generated Al particulates on the growth of the a-C films is demonstrated in Fig. 4, which presents the Raman spectra of the pure a-C film and comparative samples with the treated Al particulates. Furthermore, to acquire the bond arrangements, the Raman spectra were fitted by two Gaussian peaks after linear background subtraction, resulting in the identification of the G and D peaks.[26–28] The G and D peaks were generally attributed to the vibrations of the $sp^2$ bonded carbon atoms; the G peak originated from the stretching vibration of the $sp^2$ atoms in the rings and chains, whereas the D peak resulted from the breathing vibration of the $sp^2$ atoms only in the rings [29,30]. The fitted

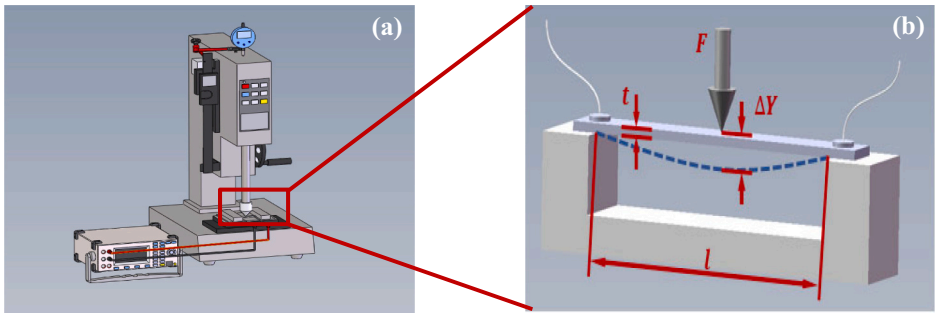


**Fig. 2.** (a) 3D schematic diagram of the home-made gauge factor testing device, and (b) enlarged photograph of the testing sample region.

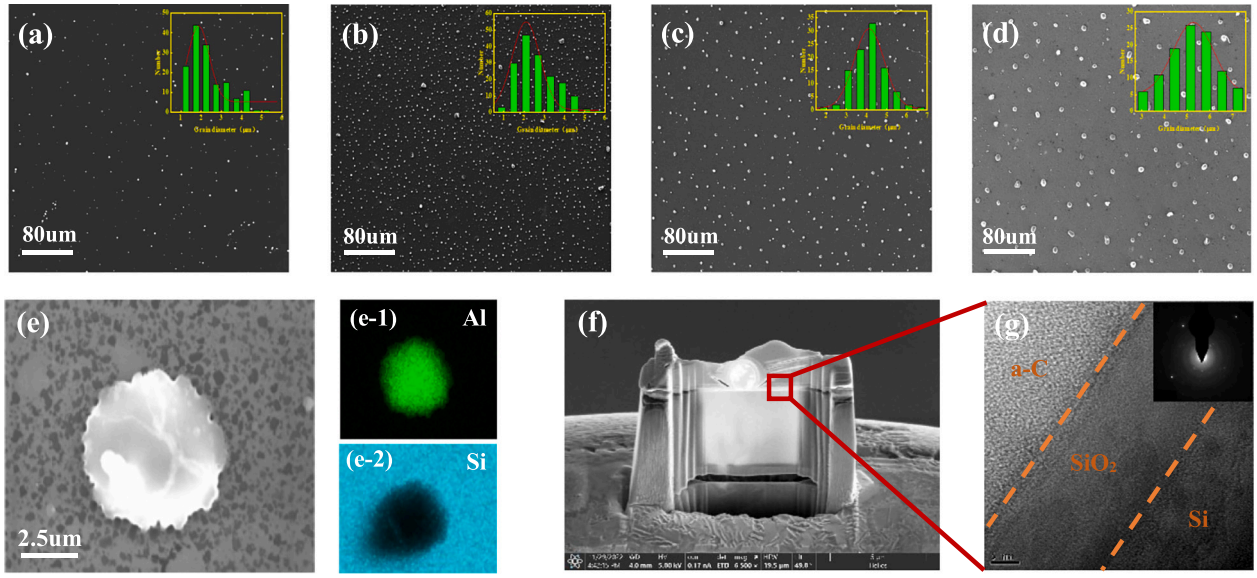


**Fig. 3.** SEM images of (a) S2, (b) S3, (c) S4, (d) and S5 after annealing, and the corresponding diameter of the Al particulate. (e) EDS mapping spectrum of the Al particulate. (f) TEM of sample prepared by FIB. (g) HRTEM and SAED of sample.

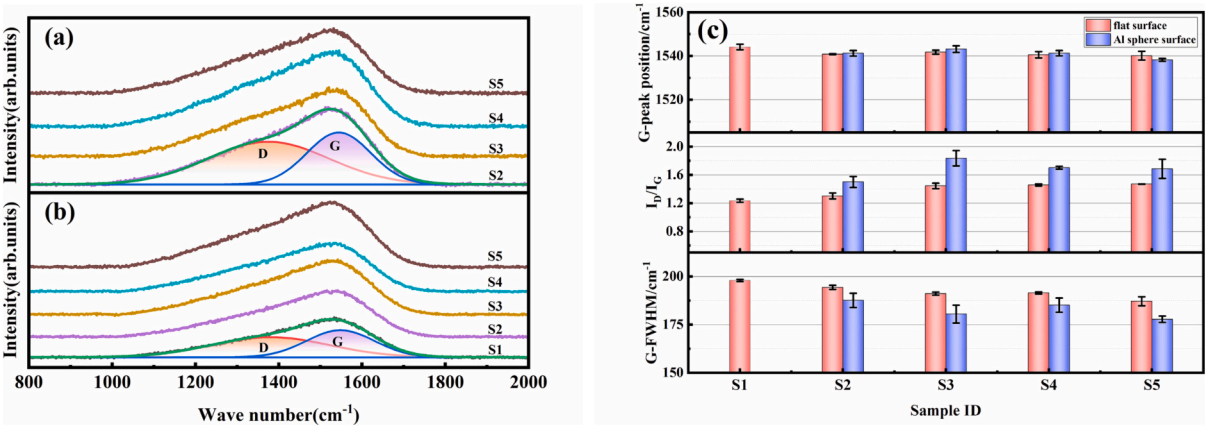


**Fig. 4.** (a) Raman results of a-C films on the surface of Al particulates. (b) Raman results of a-C films on a flat surface. (c) The fitting results of $I_D/I_G$, G-FWHM and G peak position at different positions of S1-S5 samples.

G peak position, peak area ratio $I_D/I_G$, and full width at half maximum of the G peak (G-FWHM) at different positions of various samples are shown in Fig. 4c, which reflect the degree of carbon atom disorder, $sp^2$/$sp^3$ ratio, and $sp^2$ cluster size [31]. For the plane region shown in Fig. 4c, when the thickness of the Al film increased from samples S1 to S5, the G-peak position remained stable at approximately 1540 $cm^{-1}$, whereas $I_D$/

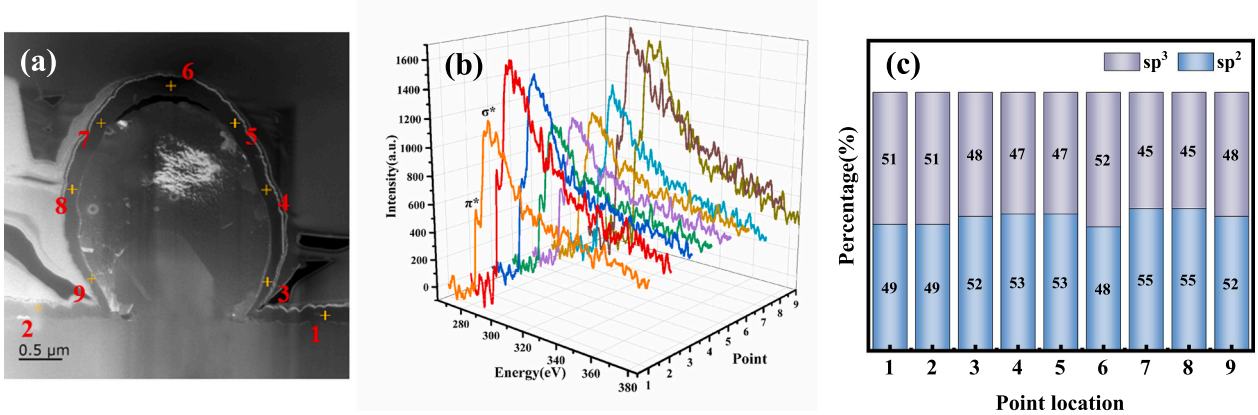


**Fig. 5.** (a) STEM image of the S3 samples. (b) EELS spectra at different areas indicated by 1–9. (c) Fitting results of the "two-window method".

$I_G$ increased from 1.26 to 1.47 and G-FWHM was significantly lower. When the Al particulates were incorporated, the $I_D/I_G$ ratio was higher than that of the flat surface, and G-FWHM further decreased. The results demonstrated that the Al particulates were beneficial for increasing the size of the $sp^2$ clusters and reducing the structural disorder of the carbon matrix.

Considering the complexity of the deposition process, the microstructural evolution of the a-C film around the Al particulates was also investigated using EELS. As shown in Fig. 5a, nine areas of interest were marked on sample S3: the flat surface (1 and 2), bottom of the spherical surface (3 and 9), middle of the spherical surface (4 and 8), upper part of the spherical surface (5 and 7), and top part of the spherical surface (6). Using EELS [32,33], the $sp^2$ and $sp^3$ content in the a-C film can be confirmed by the C—K edge spectrum ranging between 280 and 305 eV [34,35]. C-atoms with $sp^2$-hybridization exhibited a characteristic pre-peak in the EELS spectra near 285 eV, which was associated with the excitation of the 1 s core level electrons into the π* states [36]. Both, $sp^3$ and $sp^2$-hybridized C-atoms demonstrated a significant signal loss at approximately 290 eV, which was related to the excitation of the 1 s electron into the σ* states [34]. Therefore, the $sp^3/sp^2$ ratio was extracted by the π* and σ* peak area intensities and compared to the value of graphite [37]. Fig. 5b-c present the EELS results for each test position. Note, the $sp^2$ content of a-C on the flat surface was approximately 49 %, whereas that on the spherical surface was generally higher, ranging between 53 and 55 %. Therefore, Al particulates can be concluded to facilitate the local graphitization of amorphous carbon films.

### 3.2. Electrical properties and GF test

Fig. 6a-e illustrate the I-V plots of the S1–S5 samples at temperatures ranging between 200 and 400 K. Overall, the I-V characteristics of all the test samples were highly symmetric in all the temperature ranges. Moreover, under a certain excitation current, the corresponding voltage of each sample decreased as the test temperature increased, indicating typical semiconductor behavior [38,39]. In addition, S1 exhibited a nearly linear I-V characteristic within this temperature range, suggesting its typical ohmic behavior, whereas S2–S5 presented typical non-ohmic behavior with nonlinear I-V plots at a low temperature of 200 K, suggesting the presence of a Schottky contact between the Al particulate and a-C films. Considering the test data under 300 K as an example, the resistivity consistently decreased from 0.324 Ω·mm to 0.126 Ω·mm as the thickness of the Al film increased, as shown in Fig. 6f, which may be attributed to the increase in the conductive Al and $sp^2$ phase content.

Fig. 7a presents the R-T plots of the five samples within 200–400 K. As the temperature increased, the resistivity of all the samples monotonically decreased; however, the variation was more pronounced in samples with a higher initial resistivity. For example, the resistivity of S1 decreased from 1.596 Ω·mm to 0.128 Ω·mm when the temperature increased from 200 K to 400 K, with a reduction ratio of 92 %. Similarly, the resistivity of the S5 sample decreased by 89.5 %, from 0.416 Ω·mm at 200 K to 0.044 Ω·mm at 400 K. The TCR values were determined from the R-T plots using Eq. (2) [40]:

$$TCR = \frac{\rho - \rho_0}{\rho_0} \times \frac{1}{T - T_0} \times 10^6 \quad (2)$$

where $\rho$ and $\rho_0$ represent the resistivity at temperatures $T$ and $T_0$, respectively. Fig. 7b displays the TCR values for each sample. The absolute value of the TCR monotonically decreased from −4625 ppmK-1 to −4460 ppmK-1 when the thickness of the Al film increased from samples S1 to S5, indicating that the resistivity and TCR of a-C films can be decreased by adding Al particulates to the a-C films.

The carrier transport mechanism in the a-C film was analyzed by fitting the R-T curves. Unlike free electrons in crystalline semiconductors, localized electrons in amorphous semiconductors can only be conducted via tunnelling or thermal activation [41]. Consequently, these electrons in distinct states may display diverse transport mechanisms at different temperature ranges, resulting in versatile electrical properties [42]. The R-T curve of an amorphous semiconductor satisfies the following Eq. (3) [43,44]:

$$R = R_{ct} exp\left(\frac{T_{ct}}{T}\right)^n \quad (3)$$

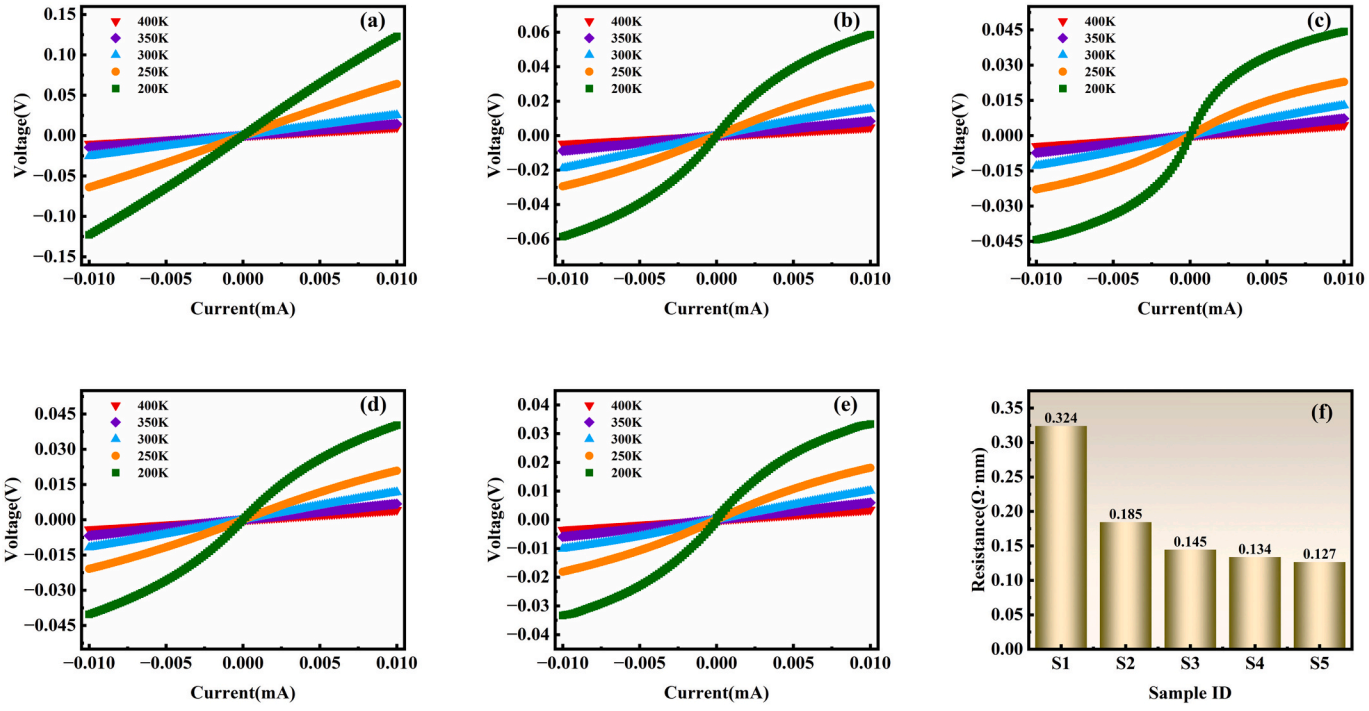


**Fig. 6.** (a)-(e) I—V characteristic plot of samples S1–S5 from 200 K to 400 K. (f) Electrical resistivity of samples S1-S5 at 300 K.

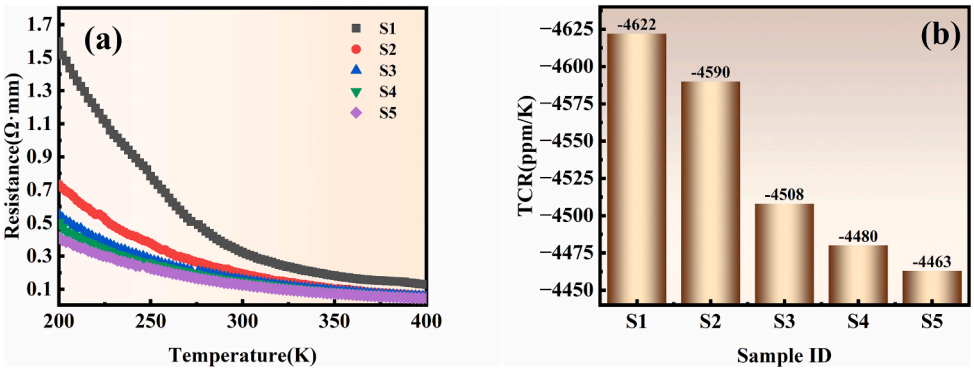


**Fig. 7.** (a) R-T behaviors of samples S1–S5 from 200 K to 400 K. (b) TCR of samples S1–S5.

where $R_{ct}$ and $T_{ct}$ are constants, $R_{ct}$ is the pre-exponential index, and $T_{ct}$ is the characteristic temperature related to the activation energy. The value of n varies depending on the electron-transport system. Here, $n = 1$ indicates that the electron transport mechanism is based on thermal activation, which usually corresponds to a higher temperature range, n = 1/2 corresponds to the two-dimensional program transition conduction of the Efros-Shklovskii (ES) type, where the influence of the Coulomb interaction between the carriers should be considered, and n = 1/4 corresponds to a Mott-type three-dimensional variable-range hopping (VRH) electron transport mechanism.

Because the thickness of the Al particulates was several tens of times larger than that of the a-C film, the a-C films with micron-scale Al particulates can be simplified as composites. Compared with the ES type mechanism, the electrical behavior of the subject was more appropriately described using the three-dimensional VRH process, where n = 1/4. Fig. 8a-b present the fitting results of samples S1-S5 at temperatures ranging between 200 and 400 K. Note, all five samples exhibited two primary electron transport mechanisms over the entire range of test temperatures. For example, the ln(R) values of S1 exhibited a linear relationship with $T^{-1/4}$ between 200 K and 245 K, suggesting that VRH conduction was the predominant mechanism within these temperatures. However, from 245 K to 400 K, a linear relationship was observed between ln(R) and $T^{-1}$, indicating that thermal activation was dominant at higher temperatures. Similarly, S2-S5 demonstrated an analogous electron transport mechanism, and compared with S1, the VRH process of the S2-S5 samples had a larger temperature range of up to 300 K.

According to the energy band theory, the carrier transfer between the Al particulates and a-C films was closely related to their work function, which can be determined by ultraviolet photoelectron spectroscopy (UPS). The photoelectron spectra based on the acquired binding energy and electron count rate are displayed in Fig. 9. By identifying the secondary electron cut-off (SECO) energy and Fermi level positions in the diagram, the work function $W_F$ can be obtained using the following Eq. (4) [45]:

$$W_F = hv - \left(E_{cutoff} - E_F\right) \tag{4}$$

where $hv$ is the energy of the incoming photons (21.22 eV) emitted by the Helium (He) I discharge lamp, $E_{cutoff}$ is the secondary electron cutoff energy, and $E_F$ is the Fermi level.

As illustrated in Fig. 9, the measured secondary electron cutoff energy was 16.51 eV. Because UPS directly considers the Fermi level as the energy reference point, if no bias was applied to the sample during the measurement, the binding energy EB = 0 corresponds to the Fermi level $E_F$. Therefore, the $W_F$ value of a-C film was 4.71 eV in this study. Simultaneously, the energy maximum ($E_v$) of the valence band with respect to the Fermi level ($E_F$) of the a-C film can be identified from the UPS spectrum. The point of intersection with the background intensity level was considered as the valence band edge [46]. Here, the bandgap between $E_V$ and $E_F$ was 1.26 eV.

The UV–visible diffuse reflection spectrum was employed to further determine the location of the Fermi level of a-C within the energy band. Fig. 10a presents the reflectance curve of the a-C film; the reflectance

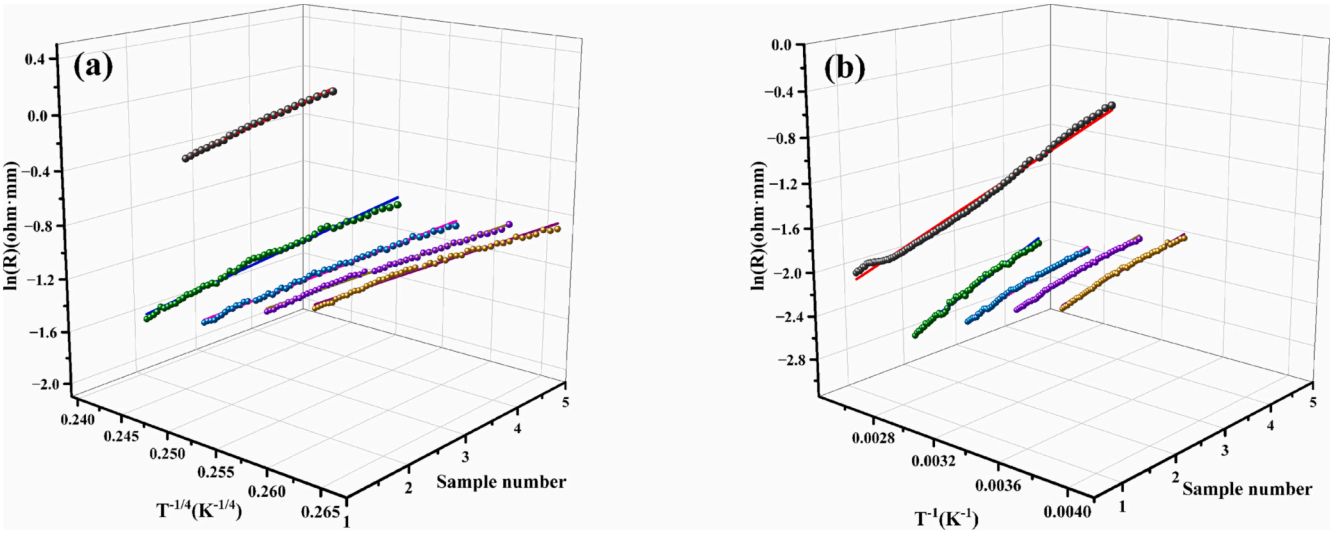


**Fig. 8.** Relationship between (a) ln(R) and $T^{-1/4}$, and (b) $T^{-1}$, at different temperature ranges for samples S1–S5. The red lines indicate the fitting results. (For interpretation of the references to color in this figure legend, the reader is referred to the web version of this article.)

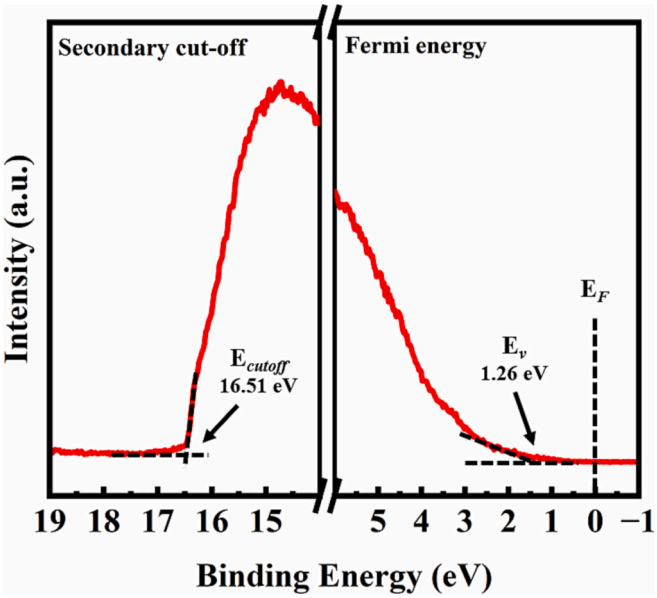


**Fig. 9.** UPS spectra of the a-C film.

data was converted to the absorption coefficient F(R) using the Kubelka-Munk Eq. (5) [47]:

$$F(R) = \frac{(1-R)^2}{2R} \tag{5}$$

where R denotes the reflectivity of the a-C film. Based on the obtained absorption coefficient F(R), the optical bandgap energy was calculated using the Eq. (6) [48]:

$$[hv^*F(R)]^{\frac{1}{n}} = A(hv - E_g) \tag{6}$$

where $hv$ is the photon energy, $E_g$ is the optical band gap energy, A is a constant, and $n$ corresponds to the semiconductor material and type of transition. For direct-bandgap semiconductors, $n = 1/2$; for indirect-bandgap semiconductors, $n = 2$. Pandey and Majeed indicated that a-C is a direct bandgap semiconductor [48,49]. Therefore, in this study, $n = 1/2$. Fig. 10b demonstrates the $[hv \times F(R)]^2$-$hv$ curve of the a-C film. According to the photon energy obtained from the extrapolation of the linear portion of the curve to F(R) = 0, the optical bandgap energy of the a-C film was deduced to be approximately 3.88 eV.

KPFM is a measurement technique based on atomic force microscopy (AFM) that can be used to investigate the surface potential [50,51]. Here, the role of Al particulates on the conductive paths and potential of the a-C film surface was investigated. Fig. 11 illustrates the variation in the electric potential on the surface of sample S3. Fig. 11a demonstrates the AFM image of the a-C film in tapping mode, with a scanning area of 50 μm × 50 μm, in which the micron-scale Al particulates had a similar size and height. Fig. 11b presents the corresponding KPFM image of the a-C film, where the color represents the variation in the charge-carrier density [52]. Generally, an oscillating conductive probe applies an AC voltage while scanning the sample surface to detect the change in the electrostatic force between the tip and test sample, which is caused by local changes in the surface potential. To minimize the detected electrostatic force, a DC bias was applied to offset the contact potential difference ($V_{CPD}$) between the tip and sample at each point of the scan. The distribution of the surface-potential of the sample was then reconstructed using the KPFM signal based on the applied DC bias. Based on the obtained $V_{CPD}$ between the probe tip and sample, the surface potential of the sample can be calculated using Eq. (7) [53,54].

$$\Phi_{sample} = \Phi_{tip} - eV_{CPD} \tag{7}$$

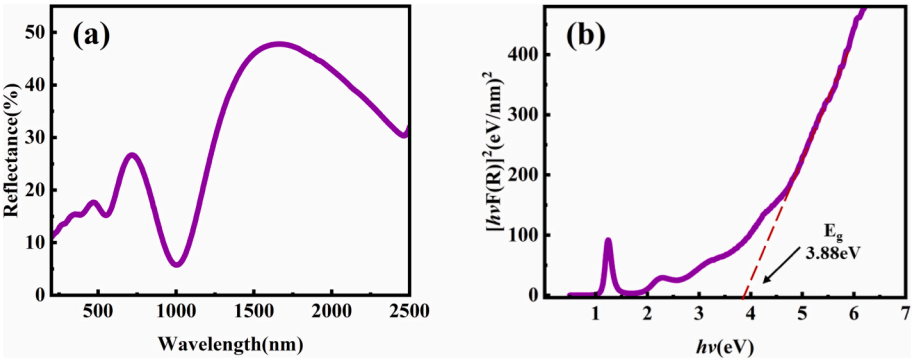


**Fig. 10.** (a) Reflectance curve. (b) $[hv^*F(R)]^2$-hv curve of the a-C film.

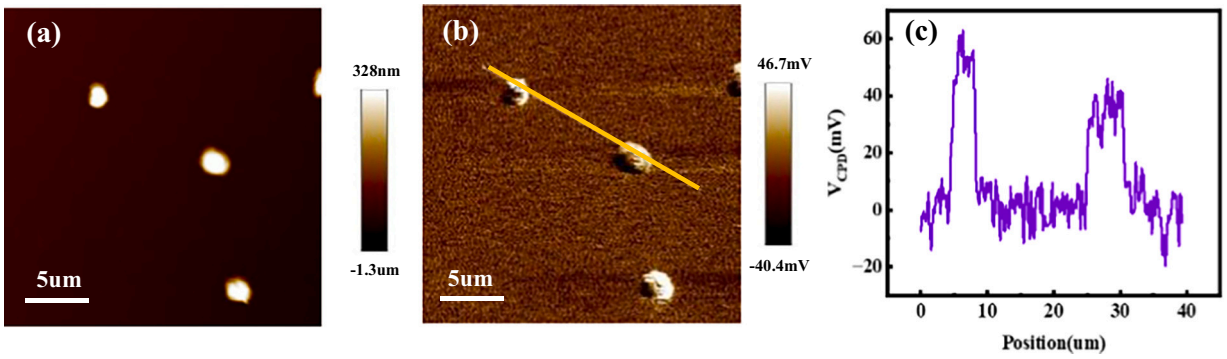


**Fig. 11.** KPFM reveals the variation of the surface potential at different positions of the a-C films. (a) Tapping mode AFM images. (b) KPFM potential images of the a-C film. (c) $V_{CPD}$ profile at the underline.

Here, $\Phi_{sample}$ and $\Phi_{tip}$ are the surface potential of the sample and work function of the probe tip, respectively. Generally, a brighter contrast of the scanning probe image indicates a higher positive voltage and larger $V_{CPD}$ of the sample [55,56].

As illustrated in Fig. 11b, the a-C film coated on the Al particulates demonstrated brighter KPFM images compared to the other regions. Furthermore, the maximum $V_{CPD}$ of the composite a-C film was estimated to be 62.8 mV (Fig. 11c), whereas $\Phi_{sample}$ was approximately 5.33 eV, demonstrating a lower potential and more conductive activities compared with other regions. Specifically, the tip of the probe was coated with Pt—Ir and its $\Phi_{tip}$ was 5.4 eV [57]. As a result, the introduction of Al particulates led to a better conductivity in the a-C film owing to the current preferentially passing through the lower potential; this may have originated from the promotion of the $sp^2$ bonds in the a-C film with the Al particulates, which offered the conductive channels for better conductivity.

Fig. 12 presents the GF values of the five samples. Compared with S1, as the density of the Al particulates increased to the maximum value in S3, the GF of the a-C film gradually increased from the minimum (8.2) to the maximum value (36.9). Conversely, the GF exhibited a rapid decline when the density of the Al particulates decreased.

### 3.3. Discussion of Piezoresistive mechanisms

According to the SEM, TEM, and HRTEM images, the Al film was completely dewetted after annealing. Consequently, the test samples can be regarded as composite structures, considering the distribution of the $sp^2$ clusters and micron-scale Al particulates in the amorphous carbon matrix.

Introducing the Al particulates changed the I-V plots from demonstrating an ohmic contact to a non-ohmic contact, especially in the low-temperature range, which can be explained by the Schottky barrier owing to the metal-semiconductor contacts. Only high-energy carriers passed the Schottky barrier to transmit between the Al metal and a-C. Therefore, increasing the voltage caused the carriers to obtain more energy across the Schottky barrier and thus changed the current flowing through the sample, resulting in the non-ohmic contact [58].

The R-T curves demonstrate that all the test samples exhibited semiconductor properties, and the TCR progressively declined. In addition, the relationship between ln (R) and $(1/T)^n$ revealed the presence of thermal activation at high temperatures and three-dimensional Mott-type VRH conduction at low temperatures. When Al particulates were added, three-dimensional Mott-type VRH conduction dominated at higher temperatures ranging from 200 to 300 K. According to KPFM, the surface of the Al particulates demonstrated a lower electric potential and better electrical conductivity compared to the amorphous carbon matrix. Consequently, the conductive path across the Al particulate and a-C film interface is critical for determining the electrical and piezoresistive properties.

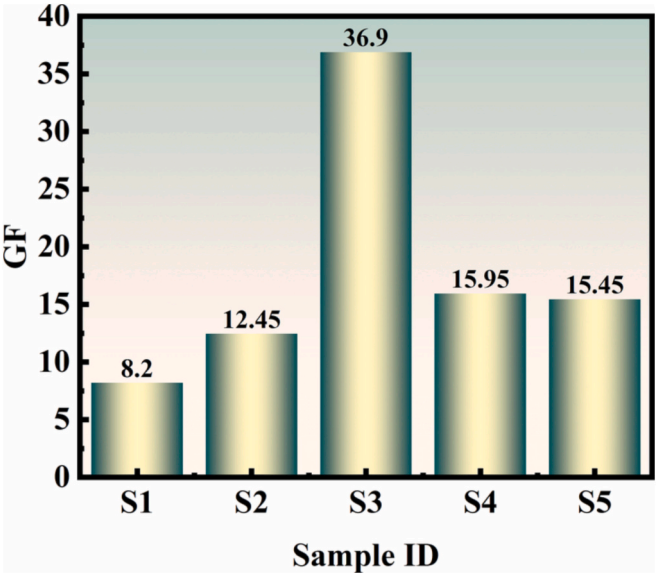


**Fig. 12.** GF testing results of different samples.

Based on the aforementioned structural and electrical characteristics, a model explaining the corresponding piezoresistive effects was proposed, as illustrated in Fig. 13. After the introduction of Al particulates into the a-C films, a Schottky potential barrier was formed at the contact interface between the Al metal and a-C. Therefore, this potential barrier can be regarded as a potential tunnelling barrier. According to the UV–visible diffuse reflection and UPS spectra, the optical bandgap of the a-C film was 3.88 eV, and the bandgap between $E_F$ and $E_V$ was 1.26 eV. Consequently, hole conduction have played a dominant role in the carrier transport. Because the work function of the a-C film was 4.71 eV and that of Al was 4.28 eV, the energy band of the a-C film bent downward to generate a P-type barrier layer, which formed a potential barrier with a height of 0.43 eV and acted as a barrier to the carrier transport. The band structure of a semiconductor changes under an external strain [59–61]. Consequently, this distorted band structure may directly affect carrier tunnelling between the metal and semiconductor. Sample S3 exhibited the highest density of the micron-scale Al particulates and Al/a-C interfaces, resulting in the largest resistance change, that is, a noticeable piezoresistive effect.

## 4. Conclusion

A composite structure composed of Al particulates added to an amorphous carbon matrix was studied. The Al film deposited by the DCMS technique was dewetted by an annealing process. Subsequently, HiPIMS was used to deposit the a-C films. The density and size of the Al particulates was adjusted by varying the thickness of the Al film.

Investigations of these films demonstrated the feasibility of improving their piezoresistive properties by actively regulating the size and distribution of metal particulates in an amorphous carbon matrix. A high GF of 36.9 combined with a TCR of −4508 ppm/K was obtained at the highest Al particulate density, which improved the GF while decreasing the TCR.

The structures, electrical characteristics, and optical bandgaps of the films were investigated to gain a deeper understanding of the underlying physical effects on the material. These results indicate that Al particulates facilitated the formation of $sp^2$ bonds in a-C. Additionally, the $sp^2$ content of a-C on the surface of the Al particulates was approximately 5 % higher than that in other areas. Simultaneously, the electric potential was lower at this position, which changed the initial conduction pathway. At the Al/a-C contact interface, a Schottky barrier of 0.43 eV was formed, in which the hole achieved carrier transport by tunnelling. Therefore, the height of the barrier was concluded to be a crucial factor in the tunnelling process, and the change in the barrier under excessive stress resulted in the piezoresistive effect. The synthesis of these results led to a simple carrier transport model, which helped in understanding the correlations between the material structure and piezoresistive properties.

## CRediT authorship contribution statement

**Shanze Liu:** Writing – original draft, Visualization, Validation, Investigation, Formal analysis, Data curation, Conceptualization. **Zhihan Zhao:** Investigation, Formal analysis, Data curation. **Wenlong Zhang:** Investigation, Data curation. **Rende Chen:** Methodology, Investigation. **Jing Wei:** Writing – review & editing. **Peng Guo:** Writing – review & editing, Visualization, Project administration, Investigation, Funding acquisition, Conceptualization. **Aiying Wang:** Writing – review & editing, Visualization, Resources, Project administration, Funding

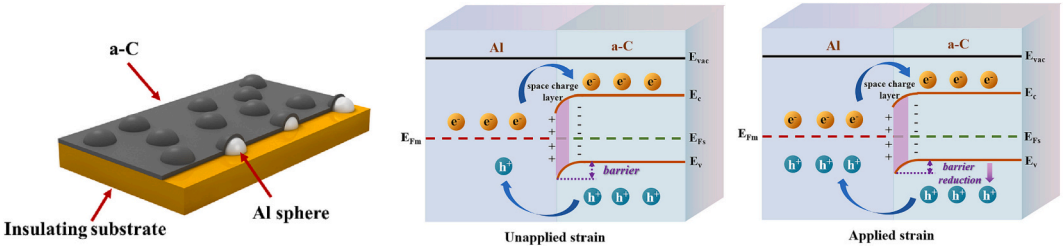


**Fig. 13.** Schematic diagram of the piezoresistive mechanism.

acquisition.

## Declaration of competing interest

The authors declare that they have no known competing financial interests or personal relationships that could have appeared to influence the work reported in this paper.

## Data availability

Data will be made available on request.

## Acknowledgements

This work was financially supported by Science and Technology Innovation 2025 Major Project of Ningbo (2020Z023), National Natural Science Foundation of China (U20A20296, 52205237, 52127803).

## References

[1] A.S. Fiorillo, C.D. Critello, S.A. Pullano, Theory, technology and applications of piezoresistive sensors: A review, Sensors Actuators A Phys. 281 (2018) 156–175, https://doi.org/10.1016/j.sna.2018.07.006.
[2] M.A. Fraga, H. Furlan, R.S. Pessoa, M. Massi, Wide bandgap semiconductor thin films for piezoelectric and piezoresistive MEMS sensors applied at high temperatures: an overview, Microsyst. Technol. 20 (2013) 9–21, https://doi.org/10.1007/s00542-013-2029-z.
[3] J. Robertson, Diamond-like amorphous carbon, Mater. Sci. Eng. (2002) 129–281, https://doi.org/10.1016/S0927-796X(02)00005-0.
[4] A. Catena, Q. Guo, M.R. Kunze, S. Agnello, F.M. Gelardi, S. Wehner, C.B. Fischer, Morphological and chemical evolution of gradually deposited diamond-like carbon films on polyethylene terephthalate: from subplantation processes to structural reorganization by intrinsic stress release phenomena, ACS Appl. Mater. Interfaces 8 (2016) 10636–10646, https://doi.org/10.1021/acsami.6b02113.
[5] R. Zhu, Q. Tao, M. Lian, X. Feng, J. Liu, M. Ye, X. Wang, S. Dong, T. Cui, P. Zhu, Modulating band gap of boron doping in amorphous carbon Nano-film, Materials (Basel) 12 (2019), https://doi.org/10.3390/ma12111780.
[6] L. AH., Applications of diamond-like carbon thin films. Carbon: An International Journal Sponsored by the American Carbon Society, 36 (1998) 555–560, doi: https://doi.org/10.1016/S0008-6223(98)00062-1.
[7] A.A. Al-Azizi, O. Eryilmaz, A. Erdemir, S.H. Kim, Nano-texture for a wear-resistant and near-frictionless diamond-like carbon, Carbon 73 (2014) 403–412, https://doi.org/10.1016/j.carbon.2014.03.003.
[8] M. Petersen, R. Bandorf, G. Bräuer, C.P. Klages, Diamond-like carbon films as piezoresistors in highly sensitive force sensors, Diam. Relat. Mater. 26 (2012) 50–54, https://doi.org/10.1016/j.diamond.2012.04.004.
[9] E. Peiner, A. Tibrewala, R. Bandorf, S. Biehl, H. Lüthje, L. Doering, Micro force sensor with piezoresistive amorphous carbon strain gauge, Sensors Actuators A Phys. 130-131 (2006) 75–82, https://doi.org/10.1016/j.sna.2005.11.059.
[10] A. Tibrewala, E. Peiner, R. Bandorf, S. Biehl, H. Lüthje, Longitudinal and transversal piezoresistive effect in hydrogenated amorphous carbon films, Thin Solid Films 515 (2007) 8028–8033, https://doi.org/10.1016/j.tsf.2007.03.046.
[11] Š. Meškinis, R. Gudaitis, V. Kopustinskas, S. Tamulevičius, Electrical and piezoresistive properties of ion beam deposited DLC films, Appl. Surf. Sci. 254 (2008) 5252–5256, https://doi.org/10.1016/j.apsusc.2008.02.037.
[12] A. Tibrewala, E. Peiner, R. Bandorf, S. Biehl, H. Lüthje, The piezoresistive effect in diamond-like carbon films, J. Micromech. Microeng. 17 (2007) S77–S82, https://doi.org/10.1088/0960-1317/17/7/s03.
[13] A. Tibrewala, E. Peiner, R. Bandorf, S. Biehl, H. Lüthje, Transport and optical properties of amorphous carbon and hydrogenated amorphous carbon films, Appl. Surf. Sci. 252 (2006) 5387–5390, https://doi.org/10.1016/j.apsusc.2005.12.046.
[14] J. Zhou, P. Guo, L. Cui, C. Yan, D. Xu, F. Li, C. Zhang, A. Wang, Wrinkled and cracked amorphous carbon film for high-performance flexible strain sensors, Diam. Relat. Mater. 132 (2023), https://doi.org/10.1016/j.diamond.2022.109619.
[15] X. Ma, Q. Zhang, P. Guo, H. Li, Y. Zhao, A. Wang, Self-supporting ultrathin DLC/Si3N4/SiO2 for Micro-pressure sensor, IEEE Sensors J. 22 (2022) 3937–3944, https://doi.org/10.1109/jsen.2021.3133935.
[16] S. Biehl, C. Rumposch, G. Bräuer, H.-W. Hoffmeister, M. Luig, Development of a novel piezoresistive thin film sensor system based on hydrogenated carbon, Microsyst. Technol. 20 (2014) 989–993, https://doi.org/10.1007/s00542-014-2101-3.
[17] Š. Meškinis, R. Gudaitis, A. Vasiliauskas, A. Čiegis, K. Šlapikas, T. Tamulevičius, M. Andrulevičius, S. Tamulevičius, Piezoresistive properties of diamond like carbon films containing copper, Diam. Relat. Mater. 60 (2015) 20–25, https://doi.org/10.1016/j.diamond.2015.10.007.
[18] M. Grein, R. Bandorf, K. Schiffmann, G. Bräuer, Material structure and piezoresistive properties of niobium containing diamond-like-carbon films, Surf. Coat. Technol. 357 (2019) 273–279, https://doi.org/10.1016/j.surfcoat.2018.10.008.
[19] R. Koppert, D. Goettel, O. Freitag-Weber, G. Schultes, Nickel containing diamond like carbon thin films, Solid State Sci. 11 (2009) 1797–1800, https://doi.org/10.1016/j.solidstatesciences.2009.04.022.
[20] R. Koppert, S. Uhlig, H. Schmid-Engel, D. Göttel, A.-C. Probst, G. Schultes, U. Werner, Structural and physical properties of highly piezoresistive nickel containing hydrogenated carbon thin films, Diam. Relat. Mater. 25 (2012) 50–58, https://doi.org/10.1016/j.diamond.2012.01.031.
[21] S. Bhattacharyya, S.R.P. Silva, Transport properties of low-dimensional amorphous carbon films, Thin Solid Films 482 (2005) 94–98, https://doi.org/10.1016/j.tsf.2004.11.125.
[22] S.W. Hieke, G. Dehm, C. Scheu, Annealing induced void formation in epitaxial Al thin films on sapphire (α-Al2O3), Acta Mater. 140 (2017) 355–365, https://doi.org/10.1016/j.actamat.2017.08.050.
[23] S.W. Hieke, B. Breitbach, G. Dehm, C. Scheu, Microstructural evolution and solid state dewetting of epitaxial Al thin films on sapphire (α-Al2O3), Acta Mater. 133 (2017) 356–366, https://doi.org/10.1016/j.actamat.2017.05.026.
[24] C.V. Thompson, Solid-state Dewetting of thin films, Annu. Rev. Mater. Res. 42 (2012) 399–434, https://doi.org/10.1146/annurev-matsci-070511-155048.
[25] X. Ma, X. Tong, P. Guo, Y. Zhao, Q. Zhang, H. Li, R. Chen, A. Wang, MEMS piezoresistive force sensor based on DC sputtering deposited amorphous carbon films, Sensors Actuators A Phys. 303 (2020), https://doi.org/10.1016/j.sna.2019.111700.
[26] K. Takahashi, M. Tonouchi, Influence of Mn doping on ferroelectric-Antiferromagnet BiFeO3Thin films grown on (LaAlO3)0.3(Sr2AlTaO6) 0.7Substrates, Jpn. J. Appl. Phys. 45 (2006) L755–L757, https://doi.org/10.1143/jjap.45.L755.
[27] H.X. Li, T. Xu, J.M. Chen, H.D. Zhou, H.W. Liu, The effect of applied dc bias voltage on the properties of a-C:H films prepared in a dual dc–rf plasma system. Appl. Surf. Sci., 227 (2004) 364–372, doi:https://doi.org/10.1016/j.apsusc.2003.12.013.
[28] P. Guo, X. Li, L. Sun, R. Chen, P. Ke, A. Wang, Stress reduction mechanism of diamond-like carbon films incorporated with different cu contents, Thin Solid Films 640 (2017) 45–51, https://doi.org/10.1016/j.tsf.2017.09.001.
[29] W.A. Eurídice, N.B. Leite, R.V. Gelamo, P.A. de Almeida Buranello, M.V. da Silva, C.J.F. de Oliveira, R.F.V. Lopez, C.N. Lemos, A. de Siervo, J.A. Moreto, a-C:H films produced by PECVD technique onto substrate of Ti6Al4V alloy: Chemical and biological responses. Appl. Surf. Sci., 503 (2020), doi:https://doi.org/10.1016/j.apsusc.2019.144084.
[30] E. Mohagheghpour, M. Rajabi, R. Gholamipour, M.M. Larijani, S. Sheibani, Correlation study of structural, optical and electrical properties of amorphous carbon thin films prepared by ion beam sputtering deposition technique, Appl. Surf. Sci. 360 (2016) 52–58, https://doi.org/10.1016/j.apsusc.2015.10.213.
[31] P.K. Chu, L. Li, Characterization of amorphous and nanocrystalline carbon films, Mater. Chem. Phys. 96 (2006) 253–277, https://doi.org/10.1016/j.matchemphys.2005.07.048.
[32] J. Xie, K. Komvopoulos, The effect of argon ion irradiation on the thickness and structure of ultrathin amorphous carbon films, J. Appl. Phys. 119 (2016), https://doi.org/10.1063/1.4942440.
[33] N. Brodusch, H. Demers, A. Gelle, A. Moores, R. Gauvin, Electron energy-loss spectroscopy (EELS) with a cold-field emission scanning electron microscope at low accelerating voltage in transmission mode, Ultramicroscopy 203 (2019) 21–36, https://doi.org/10.1016/j.ultramic.2018.12.015.
[34] X. Zhang, R. Schneider, E. Müller, D. Gerthsen, Practical aspects of the quantification of sp2-hybridized carbon atoms in diamond-like carbon by electron energy loss spectroscopy, Carbon 102 (2016) 198–207, https://doi.org/10.1016/j.carbon.2016.02.020.

[35] S. Gayathri, N. Kumar, R. Krishnan, T.R. Ravindran, S. Amirthapandian, S. Dash, A. K. Tyagi, M. Sridharan, Influence of transition metal doping on the tribological properties of pulsed laser deposited DLC films, Ceram. Int. 41 (2015) 1797–1805, https://doi.org/10.1016/j.ceramint.2014.09.125.
[36] A.-Y. Wang, K.-R. Lee, J.-P. Ahn, J.H. Han, Structure and mechanical properties of W incorporated diamond-like carbon films prepared by a hybrid ion beam deposition technique, Carbon 44 (2006) 1826–1832, https://doi.org/10.1016/j.carbon.2005.12.045.
[37] F. Qian, R.K. Singh, S.K. Dutta, P.P. Pronko, Laser deposition of diamondlike carbon films at high intensities, Appl. Phys. Lett. 67 (1995) 3120–3122, https://doi.org/10.1063/1.114853.
[38] Z.U.D. Babar, R.-K. Zheng, M. Mumtaz, S. Rizwan, Magneto-transport of mechanically-pressed niobium carbide (Nb2C) distorted MXene, Mater. Lett. 285 (2021), https://doi.org/10.1016/j.matlet.2020.129210.
[39] H. Li, P. Guo, D. Zhang, R. Chen, X. Zuo, P. Ke, H. Saito, A. Wang, Influence of deposition temperature on the structure, optical and electrical properties of a-C films by DCMS, Appl. Surf. Sci. 503 (2020), https://doi.org/10.1016/j.apsusc.2019.144310.
[40] M. Petersen, U. Heckmann, R. Bandorf, V. Gwozdz, S. Schnabel, G. Bräuer, C.-P. Klages, Me-DLC films as material for highly sensitive temperature compensated strain gauges, Diam. Relat. Mater. 20 (2011) 814–818, https://doi.org/10.1016/j.diamond.2011.03.036.
[41] P. Stallinga, Electronic transport in organic materials: comparison of band theory with percolation/(variable range) hopping theory, Adv. Mater. 23 (2011) 3356–3362, https://doi.org/10.1002/adma.201101129.
[42] P.W. ANDERSON, Absence of diffusion in certain random lattices. Phys. Rev., 109 (1958) 1492–1505, doi:https://doi.org/10.1103/PhysRev.109.1492.
[43] C. Wan, X. Zhang, J. Vanacken, X. Gao, X. Zhang, L. Wu, X. Tan, H. Lin, V. V. Moshchalkov, J. Yuan, Electro- and magneto-transport properties of amorphous carbon films doped with iron, Diam. Relat. Mater. 20 (2011) 26–30, https://doi.org/10.1016/j.diamond.2010.11.001.
[44] C. Godet, S. Kumar, V. Chu, Field-enhanced electrical transport mechanisms in amorphous carbon films, Philos. Mag. 83 (2003) 3351–3365, https://doi.org/10.1080/14786430310001605010.
[45] T. Kamioka, Y. Hayashi, Y. Isogai, K. Nakamura, Y. Ohshita, Analysis of interface workfunction and process-induced damage of reactive-plasma-deposited ITO/SiO2/Si stack, AIP Adv. 7 (2017), https://doi.org/10.1063/1.4997495.
[46] J. Li, Z. Li, X. Liu, C. Li, Y. Zheng, K.W.K. Yeung, Z. Cui, Y. Liang, S. Zhu, W. Hu, Y. Qi, T. Zhang, X. Wang, S. Wu, Interfacial engineering of Bi2S3/Ti3C2Tx MXene based on work function for rapid photo-excited bacteria-killing, Nat. Commun. 12 (2021), https://doi.org/10.1038/s41467-021-21435-6.
[47] H. Lin, C. Huang, W. Li, C. Ni, S. Shah, Y. Tseng, Size dependency of nanocrystalline TiO2 on its optical property and photocatalytic reactivity exemplified by 2-chlorophenol, Appl. Catal. B Environ. 68 (2006) 1–11, https://doi.org/10.1016/j.apcatb.2006.07.018.
[48] S. Majeed, K. Siraj, S. Naseem, M.F. Khan, M. Irshad, H. Faiz, A. Mahmood, Structural and optical properties of gold-incorporated diamond-like carbon thin films deposited by RF magnetron sputtering, Materials Research Express 4 (2017), https://doi.org/10.1088/2053-1591/aa7430.
[49] B. Pandey, J. Mukherjee, B. Das, A.K. Kar, Nickel concentration dependent structural and optical properties of electrodeposited diamond like carbon thin films, The European Physical Journal Applied Physics 66 (2014), https://doi.org/10.1051/epjap/2014130435.
[50] D. Ziegler, J. Rychen, N. Naujoks, A. Stemmer, Compensating electrostatic forces by single-scan kelvin probe force microscopy, Nanotechnology 18 (2007), https://doi.org/10.1088/0957-4484/18/22/225505.
[51] W. Melitz, J. Shen, A.C. Kummel, S. Lee, Kelvin probe force microscopy and its application, Surf. Sci. Rep. 66 (2011) 1–27, https://doi.org/10.1016/j.surfrep.2010.10.001.
[52] A.S. Nikolenko, V.V. Strelchuk, P.M. Lytvyn, I.M. Danylenko, S.V. Malyuta, O. G. Gontar, S.P. Starik, T.V. Kovalenko, S.O. Ivakhnenko, Correlated kelvin-probe force microscopy, micro-FTIR and micro-Raman analysis of doping anisotropy in multisectorial boron-doped HPHT diamonds, Diam. Relat. Mater. 124 (2022), https://doi.org/10.1016/j.diamond.2022.108927.
[53] R. Singh, Q.A. Sial, S.-i. Han, S. Nah, J.-Y. Park, H. Seo, Nanoscale visualization of hot carrier generation and transfer at non-noble metal and oxide interface. J. Mater. Sci. Technol., 98 (2022) 151–159, doi:https://doi.org/10.1016/j.jmst.2021.04.064.
[54] W. Choi, R.K. Bera, S.W. Han, H. Park, T.W. Go, M. Choi, R. Ryoo, J.Y. Park, Doping effect of zeolite-templated carbon on electrical conductance and supercapacitance properties, Carbon 193 (2022) 42–50, https://doi.org/10.1016/j.carbon.2022.02.056.
[55] R. Kumar, D. Varandani, B.R. Mehta, Nanoscale interface formation and charge transfer in graphene/silicon Schottky junctions, KPFM and CAFM studies. Carbon 98 (2016) 41–49, https://doi.org/10.1016/j.carbon.2015.10.075.
[56] Z. Yin, R. He, Y. Chen, Z. Yin, K. Yan, K. Wang, H. Yan, H. Song, C. Yin, H. Guan, C. Luo, Z. Hu, C. Luc, Effects of surface micro–galvanic corrosion and corrosive film on the corrosion resistance of AZ91–xNd alloys, Appl. Surf. Sci. 536 (2021), https://doi.org/10.1016/j.apsusc.2020.147761.
[57] Y. Zhang, Y. Guo, L. Chen, Y. Wang, G. Zhang, Y. Zhou, Particle size and purity control study on ZrW2O8 powders using coprecipitation method, Mater. Sci. Eng. B 246 (2019) 27–33, https://doi.org/10.1016/j.mseb.2019.05.019.
[58] C. Luderer, C. Messmer, M. Hermle, M. Bivour, Transport losses at the TCO/a-Si:H/c-Si heterojunction: influence of different layers and annealing, IEEE Journal of Photovoltaics 10 (2020) 952–958, https://doi.org/10.1109/jphotov.2020.2983989.
[59] N. Katoch, A. Kumar, R. Sharma, P.K. Ahluwalia, J. Kumar, Strain tunable Schottky barriers and tunneling characteristics of borophene/MX2 van der Waals heterostructures, Phys. E. 120 (2020), https://doi.org/10.1016/j.physe.2019.113842.
[60] J. Bi, G. Wei, M. Shang, F. Gao, B. Tang, W. Yang, Piezoresistance in Si3N4 nanobelts: toward highly sensitive and reliable pressure sensors, J. Mater. Chem. C 2 (2014) 10062–10066, https://doi.org/10.1039/c4tc01810a.
[61] X. Cheng, L. Wang, F. Gao, W. Yang, Z. Du, D. Chen, S. Chen, The N and P co-doping-induced giant negative piezoresistance behaviors of SiC nanowires, J. Mater. Chem. C 7 (2019) 3181–3189, https://doi.org/10.1039/c8tc06623j.